



Povall, T.M., Govender, I. and McBride, A.T. (2021) Dense granular flows in rotating drums: a computational investigation of constitutive equations. *Powder Technology*, 393, pp. 238-249. (doi: [10.1016/j.powtec.2021.07.051](https://doi.org/10.1016/j.powtec.2021.07.051))

The material cannot be used for any other purpose without further permission of the publisher and is for private use only.

There may be differences between this version and the published version. You are advised to consult the publisher's version if you wish to cite from it.

<http://eprints.gla.ac.uk/248446/>

Deposited on 28 July 2021

Enlighten – Research publications by members of the University of  
Glasgow

<http://eprints.gla.ac.uk>

# Dense Granular Flows in Rotating Drums: A Computational Investigation of Constitutive Equations

TM Povall<sup>a,c</sup>, I Govender<sup>b,\*</sup>, AT McBride<sup>c,d</sup>

<sup>a</sup>Centre for Minerals Research, University of Cape Town, P/Bag Rondebosch, 7701

<sup>b</sup>School of Engineering, University of KwaZulu-Natal, Durban, 4041

<sup>c</sup>Centre for Research in Computational and Applied Mechanics, University of Cape Town, P/Bag Rondebosch, 7701

<sup>d</sup>Glasgow Computational Engineering Centre, The University of Glasgow, Glasgow G12 8QQ, United Kingdom of Great Britain and Northern Ireland

---

## Abstract

Novel 3D measures of compressibility and isotropy (coaxiality and collinearity) are proposed to test constitutive laws of rotating drum flows using the Discrete Element Method. In particular, the  $\mu(I)$  rheology of Jop et al. is tested. The coaxiality measure produces a lower occurrence frequency than the equivalent 2D simulation for nearly all angular separations, while the collinearity measure shows minimal deviation. The high degree of isotropy appears to be facilitated by compressibility across the downward, gravity-driven, flowing layer, and a non-zero volumetric component of the velocity gradient tensor near the bottom of the densely packed rising en-masse layer. The 3D configuration is contended to facilitate compressibility which ultimately leads to better regularisation of the equations. An empirically-derived friction law produces statistically better fits when compared to several other friction laws proposed in the literature; however, all models fail to capture the behaviour at very low inertial numbers. The failure suggests gross instability in the governing equations which is the signature of ill-posedness and/or shear banding.

*Keywords:* DEM, compressibility, isotropy, granular rheology.

---

\*Corresponding author

Email address: indresan.govender@gmail.com (I Govender)

---

## 1. Introduction

The flow of granular materials in rapidly rotating drums is often described by a free flowing, gravity-driven, layer over a densely packed rising en-masse layer that is considered static relative to the rotating drum. The equilibrium surface delineates the two flowing layers while the free surface denotes the upper boundary of the free flowing layer—see Figure 1. The gravity-driven layer exhibits a rich co-existence of flows ranging from quasi-static, near the equilibrium-surface, to rapid dense (liquid-like) flow at the free surface. The velocity in the flowing layer decreases approximately linearly with distance from the free-surface until it reaches the quasi-static region, where it decreases exponentially to zero at the equilibrium surface. Below the equilibrium surface, the velocity increases linearly with depth up to the boundary wall. The free flowing layer has particles interacting by frictional and collisional contacts [13, 7, 6]. The bulk deformation in the quasi-static (exponential) region is slow and the particles interact mostly by frictional contact [15]. Cascading and cataracting regimes will additionally have a highly-kinetic (gas-like) cataracting region above the free surface [8]. The volume of material in the gas-like region increases with rotational speed.

In two-dimensional (2D) Discrete Element Method (DEM) simulations of disks undergoing shear deformation, da Cruz et al. [5] confirmed that the state of a granular medium can be determined by the inertial number  $I$ , given by

$$I = \dot{\gamma}d\sqrt{\frac{\rho_p}{p}}, \quad (1)$$

where  $\dot{\gamma}$  is the shear rate,  $p$  is the hydrostatic pressure,  $\rho_p$  is the density of the particles and  $d$  is the particle diameter. Small values of the inertial number ( $I < 10^{-2}$ ) correspond to quasi-static flows. Likewise large values ( $I > 0.2$ )

24 correspond to the collisional (gaseous) regime. The regime of (liquid-like) dense  
 25 granular flow corresponds to the middle range of inertial numbers ( $10^{-2} < I <$   
 26  $0.2$ ). Constitutive laws are relations between kinematic and kinetic quantities.  
 27 The effective friction  $\mu$  is the ratio of the shear stress  $\tau$  and  $p$ , i.e.

$$\mu = \frac{\tau}{p}. \quad (2)$$

28 da Cruz et al. [5] found that both  $\mu$  and the packing fraction (solids fraction)  
 29  $\phi$ , which is the proportion of the total volume occupied by the particles, have a  
 30 linear dependence on  $I$ .

31 Jop et al. [10] performed experiments of particles flowing down channels of  
 32 varying width. Like da Cruz et al. [5] they found that  $\mu$  is dependent on  $I$ , but  
 33 unlike the linear dependence of da Cruz et al. [5] they found that  $\mu$  followed the  
 34 sigmoidal curve

$$\mu(I) = \mu_1 + \frac{\mu_2 - \mu_1}{I_0/I + 1}, \quad (3)$$

35 with constants  $\mu_1 = \tan(20.9^\circ)$ ,  $\mu_2 = \tan(32.76^\circ)$  and  $I_0 = 0.279$ . They also  
 36 found a linear dependence of  $\phi$  on  $I$ .

37 Jop et al. [11] generalized the constitutive law for dense granular flow to  
 38 three dimensions (3D) and used it to perform finite-difference simulations of  
 39 flow down a channel. They found that the velocity at the free surface of chute-  
 40 flow experiments agreed well with the finite-difference simulations that used the  
 41 generalized law. Two key assumptions that are necessary for the constitutive  
 42 law are:

- 43 1. The change in the packing fraction  $\phi$  is negligible, which makes the flow  
 44 incompressible.
- 45 2. The shear stress  $\boldsymbol{\tau}$  and shear rate  $\dot{\boldsymbol{\gamma}}$  tensors are scalar multiples of one  
 46 another, i. e., collinear.

47 Cortet et al. [3] performed 2D DEM simulations of a rotating drum half filled  
 48 with disks. They investigated the assumption of colinearity between the shear  
 49 stress  $\boldsymbol{\tau}$  and the deviatoric (volume preserving) part of the shear rate  $\dot{\boldsymbol{\gamma}}$  tensors  
 50 for the constitutive law of Jop et al. [11]. These quantities were obtained by  
 51 splitting the domain into a number of bins and averaging over the particles inside  
 52 each bin. The quantities in each element were averaged over 400 evenly spaced  
 53 temporal “snapshots”, which together constituted a single rotation of the drum.  
 54 In order for the colinearity condition to be satisfied, the principle directions of  $\boldsymbol{\tau}$   
 55 and  $\dot{\boldsymbol{\gamma}}$  need to be aligned. They found that the angular difference in alignment  
 56 between  $\boldsymbol{\tau}$  and  $\dot{\boldsymbol{\gamma}}$  ranged from  $-10^\circ$  to  $10^\circ$  in the flowing layer, which flows  
 57 more rapidly ( $5 \times 10^{-4} < I < 5 \times 10^{-2}$ ). In the quasi static region below the  
 58 flowing layer (with  $10^{-6} < I < 5 \times 10^{-4}$ ) the misalignment increased to  $35^\circ$ .  
 59 The misalignment is attributed to “transient dilatancy effects” in the slowly  
 60 deforming regions of the drum. They also investigated the effective friction  
 61  $\mu(I)$  of Jop et al. [11]. Despite the misalignment between  $\boldsymbol{\tau}$  and  $\dot{\boldsymbol{\gamma}}$ , the scalar  
 62 effective friction  $\mu = |\boldsymbol{\tau}|/p$  agrees reasonably well with Jop et al.’s rheology,  
 63 even in regions where the inertial number is very small ( $I \sim 10^{-5}$ ) and the  
 64 misalignment is quite large.

65 Rycroft et al. [16] performed 3D DEM simulations of tall and wide silo  
 66 drainage, as well as a pushing simulation in which half of the domain is moved  
 67 upwards. All three systems are periodic along one of their axes. They invest-  
 68 igated the applicability of continuum descriptions of flow in spatial (Eulerian)  
 69 and material (Lagrangian) settings. In data from all simulations continuum  
 70 measures were taken by averaging over rectangular volumetric elements. The  
 71 Eulerian elements were static, while the Lagrangian elements moved at the mean  
 72 velocity of the particles therein. Like Cortet et al. [3], they studied the align-  
 73 ment between the principle directions of the deviator of the shear rate and the

74 shear stress tensors. They found that the average misalignment, over a single  
75 snapshot, between the tensors was  $12^\circ$ . If the quantities were averaged over a  
76 “window” of 20 temporal snapshots the average misalignment decreased to  $6.7^\circ$ .  
77 They also found a linear relationship between the packing fraction and inertial  
78 number ( $\phi(I) = 0.635 - 8.13I$ ), which agreed with the results of da Cruz et al.  
79 [5].

80 Schaeffer [17] showed that a Coulomb material with a von Mises yield cri-  
81 terion (a threshold for the von Mises stress, an invariant measure of stress) is  
82 ill-posed sometimes in 3D and always in 2D. Barker et al. [2] showed that in 2D  
83 the  $\mu(I)$ -rheology is ill-posed for high and low inertial numbers and well-posed  
84 for intermediate values. Ill-posed in this case is defined as an instability in nu-  
85 merical solutions. They used numerical error analysis techniques to show that  
86 for a given resolution a standard numerical scheme is unstable in the ill-posed  
87 parameter space. Based on the findings of Schaeffer [17], Barker et al. [2] also  
88 suggest, but do not prove, that in 3D the  $\mu(I)$ -rheology is likely to be better  
89 posed, but “zones of ill-posedness” are still expected.

90 Lagrée et al. [12] used a numerical Navier-Stokes solver with the  $\mu(I)$ -  
91 rheology to solve 2D granular collapse problems. The numerical results were  
92 found to agree with with analytical and DEM results. Staron et al. [19] used  
93 the numerical solver of Lagrée et al. [12] to simulate 2D silo drainage. They  
94 showed that the numerical solver could be used to capture the phenomenon of  
95 a low-pressure cavity forming at the opening of the silo. Barker et al. [2] ob-  
96 served that the results of Lagrée et al. [12] and Staron et al. [19] may not display  
97 the expected zones of ill-posedness due to the ad-hoc regularisation introduced  
98 into the numerical solver to avoid a singularity at low strain rates. Recently  
99 Heyman et al. [9] showed that a slightly fluctuating compressibility regularises  
100 the  $\mu(I)$  rheology for dense granular flows by transforming the ill-posed regions

101 reported by Barker et al. [2] into well-posed regions, albeit with an unstable  
102 flow in some instances. The required compressibility was achieved by expand-  
103 ing the pressure (about the average pressure) to include amplitude-constrained  
104 variations that produced non-isochoric deformations. The constraint on the  
105 amplitude was chosen such that sufficient energy dissipation is associated with  
106 the volume changes. An interesting question that arises is whether the expected  
107 recovery of well-posed regions postulated by Barker et al. for  $3D$ —as opposed to  
108  $2D$ —simulations is actually caused by Heyman et al.’s compressibility-induced  
109 regularisation of  $\mu(I)$ -rheology equations.

110 [Key to mechanistic models of industrial granular systems such as chutes and](#)  
111 [tumbling mills is a constitutive law for granular flow.](#) The main aim of this  
112 work is to investigate the 3D constitutive law of Jop et al. by extending the  
113 ideas developed in Rycroft et al. [16] and Cortet et al. [3]. The investigation is  
114 done by assessing the results of nine 3D discrete element method simulations  
115 of a drum containing hard spheres. The isotropy assumption is assessed using  
116 a novel measure for quantifying the degree of anisotropy in the system. The  
117 compressibility assumption is assessed using the spatial gradient of the velocity.  
118 In addition, Jop et al.’s proposed form of the friction coefficient is evaluated and  
119 compared with the form proposed by da Cruz et al. [5], and a new empirically-  
120 derived form. The relationship between the packing fraction  $\phi$  and  $I$  is also  
121 explored.

122 This paper is arranged as follows. Section 2 describes the essential features  
123 of constitutive law by Jop et al. [11] that are directly utilised herein. The  
124 simulations that were performed are outlined in Section 3. In Section 4, the  
125 spatio-temporal averaging methods that were used to obtain continuum meas-  
126 ure are outlined. The compressibility of the simulated systems is examined in  
127 Section 5. In Section 6, the assumption of isotropy is assessed. The form of the

128 friction coefficient is evaluated in Section 7. The conclusion is given in Section  
 129 8.

## 130 2. The constitutive law of Jop

131 Encouraged by the predictive capabilities of the  $\mu(I)$ -based scaling laws in  
 132  $2D$  configurations, Jop et al. [11] proposed a  $3D$  constitutive model with a  
 133 view to addressing complex flows that exhibit shear in different directions. The  
 134 corresponding tensorial extension of equations (1, 2 & 3) are

$$I = \sqrt{2}|\mathbf{D}|d\sqrt{\frac{\rho p}{p}}, \quad (4)$$

$$\boldsymbol{\tau} = 2\eta(\sqrt{2}|\mathbf{D}|, p)\mathbf{D}, \quad \text{and} \quad (5)$$

$$\eta(\sqrt{2}|\mathbf{D}|, p) = \mu(I)\frac{p}{\sqrt{2}|\mathbf{D}|}, \quad (6)$$

135 where  $\eta$  is the rate-dependent effective viscosity. Jop et al. define  $\dot{\boldsymbol{\gamma}} = \mathbf{L} + \mathbf{L}^T$   
 136 and the non-standard norm  $|\dot{\boldsymbol{\gamma}}|_J = \sqrt{\frac{1}{2}\dot{\gamma}_{ij}\dot{\gamma}_{ij}} = \sqrt{2}|\mathbf{D}|$ , where  $\mathbf{v}$  denotes the  
 137 velocity with spatial gradient  $\mathbf{L} = \nabla\mathbf{v}$  and  $\nabla$  the spatial gradient operator.  
 138 The symmetric velocity gradient  $\mathbf{D} = \frac{1}{2}[\mathbf{L} + \mathbf{L}^T]$  is commonly used in con-  
 139 stitutive relations with standard norm  $|\mathbf{D}| = \sqrt{D_{ij}D_{ij}}$ . The phenomenological  
 140 relation for the effective friction coefficient  $\mu(I)$  and related constants for glass  
 141 are defined in section 1.

## 142 3. Numerical simulations

143 The simulations are done using Yet Another Dynamic Engine (Yade), an  
 144 open-source framework for modelling DEM [18].

145 The simulations model a rotating drum 450 mm in diameter with a smooth,  
 146 high friction, surface. The drum is filled to 40 % of the total volume with "glass"  
 147 beads 3 mm in diameter. The frictional, viscoelastic, contact law of Pournin  
 148 et al. [14] is used for both the beads and the drum. Pournin et al.'s contact  
 149 law is law derived from Cundall [4]. The contact law allows for particle overlap.  
 150 Figure 2 shows a diagram if two particles in contact. The force at the point of  
 151 contact between two particles is composed of functions of the scalar part of the  
 152 normal overlap  $\xi_n$  and the tangential overlap  $\xi_t$  and their time-derivatives  $\dot{\xi}_n$   
 153 and  $\dot{\xi}_t$ , i. e.

$$\mathbf{f} = \phi_n(\xi_n, \dot{\xi}_n) \mathbf{e}_n + \phi_t^C(\xi_t, \dot{\xi}_t), \quad (7)$$

154 where  $\mathbf{e}_n$  is the unit vector normal to the point of contact between the particles.  
 155  $\phi_t^C$  is governed by a Coulomb-type frictional threshold, given by

$$\phi_t^C(\xi_t, \dot{\xi}_t) = \min \left[ \mu \phi_n(\xi_n, \dot{\xi}_n), |\phi_t(\xi_t, \dot{\xi}_t)| \right] \mathbf{u}_t. \quad (8)$$

156  $\mu$  is the friction coefficient and  $\mathbf{u}_t$  is given by

$$\mathbf{u}_t = \begin{cases} \frac{\phi_t(\xi_t, \dot{\xi}_t)}{|\phi_t(\xi_t, \dot{\xi}_t)|} & \text{if } \phi_t(\xi_t, \dot{\xi}_t) \neq \mathbf{0}, \\ \mathbf{0} & \text{if } \phi_t(\xi_t, \dot{\xi}_t) = \mathbf{0}. \end{cases} \quad (9)$$

The normal  $\phi_n$  and tangential  $\phi_t$  components of the force between two particles  
 are given by

$$\phi_n(\xi_n, \dot{\xi}_n) = k_n \xi_n + c_n \dot{\xi}_n, \quad (10)$$

$$\phi_t(\xi_t, \dot{\xi}_t) = k_t \xi_t + c_t \dot{\xi}_t. \quad (11)$$

The first terms in both equations are elastic terms, and the rate dependence in  
 the second captures the viscous contribution. Pournin et al. empirically derived

analytical expressions of the parameters using data from experiments between two particles of radii  $R_1$  and  $R_2$ , whereby

$$k_n = \frac{m_{\text{eff}}}{t_c^2} (\pi^2 + \ln(\delta_n)^2), \quad (12)$$

$$c_n = \frac{2m_{\text{eff}}}{t_c} \ln(\delta_n), \quad (13)$$

$$k_t = \frac{1}{t_c^2 \left( \frac{1}{m_{\text{eff}}} + \frac{R_1^2}{I_1} + \frac{R_2^2}{I_2} \right)} (\pi^2 + \ln(\delta_n)^2), \quad (14)$$

$$c_t = \frac{1}{t_c \left( \frac{1}{m_{\text{eff}}} + \frac{R_1^2}{I_1} + \frac{R_2^2}{I_2} \right)} \ln(\delta_t), \quad (15)$$

157 where  $t_c$  is the duration of contact,  $\delta_n$  and  $\delta_t$  are, respectively, the normal  
 158 and tangential restitution coefficients, and  $m_{\text{eff}} = 1/(\frac{1}{m_1} + \frac{1}{m_2})$ . The material  
 159 parameters used for the beads and the drum are shown in Table 1. Simulations  
 160 are performed with periodic boundary conditions in the axial direction.

161 The simulations were performed for nine equally-spaced rotational speeds  
 162 ranging from 7 revolutions per minute (rpm) to 63 rpm. The set of nine simu-  
 163 lations will be referred to as the “test space”. The chosen speeds cover a wide  
 164 range of flows in the rolling and cascading regimes. For the initial state of the  
 165 system in each simulation, except the 7 rpm, a snapshot from a slower simula-  
 166 tion is used. The initial state for the 7 rpm system is an evenly-spaced grid of  
 167 particles. Each particle is imparted with a random initial velocity. In all of the  
 168 simulations a timestep of  $\Delta t = 1.23 \times 10^{-6}$  s was used.

#### 169 4. Homogenisation and feature extraction

170 Snapshots were taken of the 9 DEM simulations every 10000 timesteps. 400  
 171 snapshots were taken for each simulation. The spatio-temporal averaging for  
 172 each simulation took place as follows. The data from the 400 snapshots were  
 173 merged into 40 groups of 10 data sets. Merging 400 snapshots would be ideal,

174 but computer memory limitations made this infeasible. The spatial averaging  
 175 techniques to obtain material quantities are performed on the merged data sets.  
 176 The results of the 40 processed datasets are then averaged to obtain the final  
 177 quantities.

178 Spatial averaging is done over an array of volumetric elements with dimen-  
 179 sion  $2.5d \times 2.5d \times 8d$  inside the drum, see Figure 3. The volumetric elements  
 180 span the axis of the drum ( $8d$  in length), which makes them periodic.

181 The size of the volumetric element is small enough to resolve local effects  
 182 such as shear bands, which are typically  $10d$  to  $15d$  in size [7].

#### 183 4.1. Kinematic quantities

184 Define an averaging function  $\mathcal{G}(\mathbf{x})$  that satisfies the following conditions:

$$\int \mathcal{G}(\mathbf{x}) dV = 1 \quad \text{and} \quad \nabla \mathcal{G}(\mathbf{0}) = \mathbf{0}. \quad (16)$$

185 At time  $t$  the average density at  $\mathbf{x}$  for the set of  $N$  particles is given by

$$\rho(\mathbf{x}, t) = m \sum_{\alpha=1}^N \mathcal{G}(\mathbf{x} - \mathbf{x}^\alpha(t)). \quad (17)$$

186 Note above the use of the superscript  $\alpha$  to denote the position of the particle  
 187  $\mathbf{x}^\alpha$ . Greek superscripts are used for summations over particles. The density-  
 188 weighted average velocity is given by

$$\rho \mathbf{v}(\mathbf{x}, t) = m \sum_{\alpha=1}^N \mathbf{v}^\alpha(t) \mathcal{G}(\mathbf{x} - \mathbf{x}^\alpha(t)). \quad (18)$$

189 The velocity gradient is defined by

$$\mathbf{L} = \frac{\partial \mathbf{v}}{\partial \mathbf{x}}. \quad (19)$$

190 The velocity for each particle  $\alpha$  in the volumetric element can be approximated  
 191 using a first order Taylor approximation as

$$\mathbf{v}^\alpha \approx \mathbf{L}[\mathbf{x}^\alpha - \mathbf{x}^0] + \mathbf{v}^0, \quad (20)$$

192 where  $\mathbf{x}^0$  and  $\mathbf{v}^0$  are the averages of the position and the velocity, respectively,  
 193 of all of the particles in the volumetric element. The problem of finding the  
 194 velocity gradient thus becomes that of solving nine separate linear regression  
 195 problems, i.e. finding  $L_{ij}$  for  $i, j \in \{1, 2, 3\}$  in

$$\hat{v}_i^\alpha = L_{ij} \hat{x}_j^\alpha, \quad (21)$$

196 with  $\hat{\mathbf{x}}^\alpha = \mathbf{x}^\alpha - \mathbf{x}^0$  and  $\hat{\mathbf{v}}^\alpha = \mathbf{v}^\alpha - \mathbf{v}^0$ . Using simple linear regression, the  
 197 gradient becomes

$$L_{ij} = \frac{\sum_{\alpha=1}^N \hat{v}_i^\alpha \hat{x}_j^\alpha}{\sum_{\alpha=1}^N \hat{x}_j^\alpha \hat{x}_j^\alpha}. \quad (22)$$

#### 198 4.2. Kinetic quantities

199 The stress is given by [1]

$$\sigma_{ij}(\mathbf{x}, t) = \sigma_{ij}^k(\mathbf{x}, t) + \sigma_{ij}^c(\mathbf{x}, t), \quad (23)$$

where the kinetic stress  $\sigma_{ij}^k(\mathbf{x}, t)$  and contact stress  $\sigma_{ij}^c(\mathbf{x}, t)$  are given by

$$\sigma_{ij}^k(\mathbf{x}, t) = - \sum_{\alpha=1}^N m v_i^{\prime\alpha}(t) v_j^{\prime\alpha}(t) \mathcal{G}(\mathbf{x} - \mathbf{x}^\alpha(t)), \quad (24)$$

$$\sigma_{ij}^c(\mathbf{x}, t) = - \frac{1}{2} \sum_{\alpha, \beta, \alpha \neq \beta} f_i^{\alpha\beta}(t) x_j^{\alpha\beta}(t) \int_0^1 \mathcal{G}(\mathbf{x} - \mathbf{x}^\alpha(t) + s \mathbf{x}^{\alpha\beta}(t)) ds, \quad (25)$$

200 with  $\mathbf{x}^{\alpha\beta} = \mathbf{x}^\alpha - \mathbf{x}^\beta$  and  $\mathbf{v}^{\prime\alpha}(\mathbf{x}, t) = \mathbf{v}^\alpha(t) - \mathbf{v}(\mathbf{x}, t)$ .  $f^{\alpha\beta}$  is the force exerted by  
 201 particle  $\beta$  on particle  $\alpha$  and  $s$  is the path length of the associated line integral.

202 The kinetic stress can be interpreted as a kinetic-energy-like term, with  
 203 the contribution coming from the particles with very high velocity. Gas-like  
 204 systems will have a high kinetic stress. The contact stress arises from contact  
 205 forces between particles. Solid-like systems will have a high contact stress.  
 206 Systems with rapid-dense flow will have similar contributions from both types  
 207 of stress. [Figure 4 shows the ratio of the kinetic stress to contact stress for each](#)  
 208 [of the simulations. The contribution to the stress from the contact stress is](#)  
 209 [consistently greater than the kinetic stress, and the kinetic stress contribution](#)  
 210 [decreases sharply below the equilibrium surface. The kinetic stress increases](#)  
 211 [overall as the speed of rotation increases.](#)

## 212 5. Compressibility

213 The constitutive relation of [Jop et al.](#) requires the constitutive response of  
 214 the system to be incompressible. The volumetric component of the symmetric  
 215 velocity gradient must therefore be zero, i.e.

$$\text{tr}(\mathbf{D}) = \nabla \cdot \mathbf{v} = 0. \quad (26)$$

216 [Figure 5 shows the divergence of the velocity for each of the simulations.](#)

217 The rising layer has approximately zero divergence for the simulations. The  
 218 downward-flowing layer shows a small amount of expansion and contraction.  
 219 Expansion ( $\nabla \cdot \mathbf{v} > 0$ ) appears to occur in the upper part of the flowing layer  
 220 and a small amount of compression ( $\nabla \cdot \mathbf{v} < 0$ ) occurs in the bottom half of the  
 221 flowing layer. As the upward-flowing particles reach the maximum height and  
 222 start flowing downwards the decrease in pressure allows expansion to happen.  
 223 When the particles reach the bottom of the flowing layer the particles “behind”  
 224 them in the flowing layer exert a pressure, which compresses the region near the  
 225 edge of the drum.

226 Another way of representing the incompressibility constraint is given by

$$\mathbf{D} = \mathbf{D}_{\text{dev}}, \quad (27)$$

227 where  $\mathbf{D}_{\text{dev}}$  is the deviatoric (volume preserving) component of the symmetric  
228 velocity gradient

$$\mathbf{D}_{\text{dev}} = \mathbf{D} - \frac{1}{3}\text{tr}(\mathbf{D})\mathbf{I}. \quad (28)$$

229 The volumetric component of  $\mathbf{D}$  is therefore

$$\mathbf{D}_{\text{vol}} = \mathbf{D} - \mathbf{D}_{\text{dev}}. \quad (29)$$

230 In an incompressible system  $\mathbf{D}_{\text{vol}} = \mathbf{0}$ . The ratio of the norms of  $\mathbf{D}_{\text{vol}}$  and  
231  $\mathbf{D}_{\text{dev}}$  over the test space are shown in Figure 6.

232 Over most of the test space the contribution of  $\mathbf{D}_{\text{vol}}$  to  $\mathbf{D}$  is negligible relative  
233 to  $\mathbf{D}_{\text{dev}}$ . The area at the bottom of the drum appears to have a larger volumetric  
234 component, this becomes more pronounced for the more slowly-rotating simu-  
235 lations with a few volumetric elements having a high ratio ( $|\mathbf{D}_{\text{vol}}|/|\mathbf{D}_{\text{dev}}| \approx 1$ ).

## 236 6. Isotropy

237 In their analyses Cortet et al. [3] and Rycroft et al. [16] both compare the  
238 deviatoric  $\mathbf{D}_{\text{dev}}$ , rather than  $\mathbf{D}$ , with the shear stress  $\boldsymbol{\tau}$ . In this work the full  
239 symmetric velocity gradient  $\mathbf{D}$  is compared to  $\boldsymbol{\tau}$ , as this is a more accurate  
240 representation of Jop et al.'s rheology. Isotropy implies that the tensors  $\mathbf{D}$  and  
241  $\boldsymbol{\tau}$  are colinear. A simple test for colinearity is to check whether one tensor is  
242 a scalar multiple of the other. However, this is not useful in quantifying the  
243 extent to which two tensors are colinear. In order to quantify the isotropy of  
244 the system the colinearity requirement is split into two sub-conditions:

- 245 1. The principal directions of the tensors  $\mathbf{D}$  and  $\boldsymbol{\tau}$  must align.  
 246 2. The respective principal values of the tensors  $\mathbf{D}$  and  $\boldsymbol{\tau}$  must scale by the  
 247 same amount.

248 Both conditions need to be satisfied for the tensors to be coaxial.

### 249 6.1. Coaxiality

250 In this section condition 1, the coaxiality condition, is investigated. A new  
 251 measure of coaxiality is proposed and used. In condition 2 of Section 6.2, the  
 252 scaling condition is investigated.

253 A real-valued second-order symmetric tensor  $\mathbf{T}$  can be expressed as

$$\mathbf{T} = \sum_{i=1}^r \lambda_i \mathbf{v}_i \otimes \mathbf{v}_i, \quad (30)$$

254 where  $\lambda_1 > \dots > \lambda_r$  and  $\mathbf{v}_1, \dots, \mathbf{v}_r$  are, respectively, the principal values and  
 255 principal directions of the tensor and  $r$  is the rank of the tensor (in this case  
 256  $r = 3$ ). By definition the shear rate tensor  $\mathbf{D}$  is symmetric. Given a sufficiently  
 257 sized volumetric element, the stress  $\boldsymbol{\sigma}$ , and thus the shear component of the  
 258 stress  $\boldsymbol{\tau}$  are symmetric. The shear stress and the deformation gradient can thus  
 259 be decomposed using equation (30) as

$$\boldsymbol{\tau} = \sum_{i=1}^3 \xi_i \mathbf{t}_i \otimes \mathbf{t}_i \quad \text{and} \quad \mathbf{D} = \sum_{i=1}^3 \delta_i \mathbf{d}_i \otimes \mathbf{d}_i, \quad (31)$$

260 where  $\mathbf{d}_i$  and  $\mathbf{t}_i$  are the principal directions of  $\mathbf{D}$  and  $\boldsymbol{\tau}$ , respectively. Similarly,  
 261  $\xi_i$  and  $\delta_i$  are the respective principal values. The coaxiality condition requires  
 262 that the sets of principal directions of the shear stress  $\{\mathbf{t}_1, \mathbf{t}_2, \mathbf{t}_3\}$  and velocity  
 263 gradient  $\{\mathbf{d}_1, \mathbf{d}_2, \mathbf{d}_3\}$  coincide. Considering that the system being studied is  
 264 periodic, one of the principal directions will be approximately along the axis  
 265 of rotation of the drum. Both tensors will have the principal direction along

266 the axis, so it is ignored when testing for coaxiality. The principal directions of  
267 symmetric tensors are orthogonal to one another, so the two remaining principal  
268 directions of  $\mathbf{D}$  and  $\boldsymbol{\tau}$  will lie in the plane of rotation. The extent to which  $\mathbf{D}$   
269 and  $\boldsymbol{\tau}$  are coaxial can be quantified by comparing the angle between the two  
270 sets of principal directions of  $\mathbf{D}$  and  $\boldsymbol{\tau}$ . The measure of coaxiality is denoted  
271 by  $\theta$  and is taken to be the smallest angle between any two principal directions  
272 in the plane of rotation, as shown in the diagram in Figure 7.

273 Figure 8 shows the measure of coaxiality  $\theta$  for each volumetric element in  
274 all of the simulations that were performed. There is a region at the bottom of  
275 the drum, in the rising layer, with a large measure of coaxiality ( $\theta > 10^\circ$ ). This  
276 region gets smaller as the speed of rotation increases.

277 The downward-flowing quasi-static and rapid-dense flow regions at the top  
278 of the drum tend to have low values of the coaxiality measure ( $\theta < 10^\circ$ ). The  
279 areas with high  $\theta$  correspond to the areas where  $\mathbf{D}_{\text{vol}}$ , the volumetric component  
280 of the symmetric velocity gradient, is non-negligible (see previous section). To  
281 ensure that the compressibility of  $\mathbf{D}$  does not influence the coaxiality measure,  
282 the analyses in this section and the next were re-run with the deviatoric  $\mathbf{D}_{\text{dev}}$   
283 instead of  $\mathbf{D}$ . The results were not affected by the change.

284 Cortet et al. [3] performed DEM simulations on a two-dimensional (2D)  
285 rotating drum with the same diameter. Figure 9 shows Cortet et al.'s angular  
286 separation for a drum rotating at 12 rpm alongside the measure of coaxiality for  
287 the 14 rpm simulation that was done in this work. The results of Cortet et al.  
288 are qualitatively the same. A low measure of coaxiality ( $\theta < 10^\circ$ ) is visible in  
289 the flowing layer and a high value ( $\theta > 10^\circ$ ) is visible in the rising layer.

290 A more quantitative comparison can be done using Figure 10, which shows  
291 the normalized frequency of the coaxiality measure for the same data as in  
292 Figure 9.

293 [Cortet et al.](#)'s data has a much larger proportion of elements with high  
 294 measure of coaxiality ( $\theta > 10^\circ$ ). In order to calculate the measure of coaxiality  
 295 the principal values of both  $\boldsymbol{\tau}$  and  $\boldsymbol{D}$  must be unique. If the principal values  
 296 are not unique then the principal directions are not unique. The uniqueness of  
 297  $\xi_1$  and  $\xi_2$ , the principal values of  $\boldsymbol{\tau}$  in the plane of rotation, can be determined  
 298 by finding their normed difference  $\xi_\Delta$ , this is given by

$$\xi_\Delta = \frac{|\xi_1 - \xi_2|}{|\xi_1| + |\xi_2|}. \quad (32)$$

299 If  $\xi_\Delta \approx 0$  then  $\xi_1 \approx \xi_2$ . For all of the volumetric elements it was found that  
 300  $\xi_\Delta = 1.0$ , indicating that all of the principal values are unique and additionally  
 301 that the principal values have opposite sign (one under compression and the  
 302 other under tension). Similarly, the normed difference for the principal values  
 303 of  $\boldsymbol{D}$  is given by

$$\delta_\Delta = \frac{|\delta_1 - \delta_2|}{|\delta_1| + |\delta_2|}. \quad (33)$$

304 In all of the volumetric elements in the test space, except three in the 7 rpm sim-  
 305 ulation, the normed difference was found to be  $\delta_\Delta = 1.0$ . The three exceptions  
 306 had a non-zero normed difference ( $\delta_\Delta > 0.64$ ), so all of the principal values of  
 307  $\boldsymbol{D}$  in the test space are unique. The uniqueness of the principal values of  $\boldsymbol{\tau}$  and  
 308  $\boldsymbol{D}$  over the test space indicates that the measure of coaxiality is a meaningful  
 309 way to quantify the anisotropy.

310 The results from [Figure 8](#) show that the volumetric elements with slowly  
 311 moving particles, in the rising layer, have more anisotropy between  $\boldsymbol{D}$  and  $\boldsymbol{\tau}$ ,  
 312 this is especially pronounced for the slower simulations. The low velocity and  
 313 high pressure in the slower simulations allows local effects such as jamming and  
 314 shear banding to dominate in the rising layer. Recall that small values of the  
 315 inertial number  $I < 10^{-2}$  correspond to quasi-static flow. [Figure 11](#) shows the

316 measure of coaxiality  $\theta$  vs the inertial number  $I$  over the test space.

317 The volumetric elements in the quasi-static regime ( $I < 10^{-2}$ ) have a much  
318 lower degree of coaxiality (higher  $\theta$ ) and the rapidly flowing volumetric elements  
319 have a high degree of coaxiality.

320 The set of histograms in Figure 12 show the distribution of the measure of  
321 coaxiality  $\theta$  for each of the simulations in the test space.

322 Details on how to interpret the figure are given in the accompanying caption.  
323 The figure allows one to observe the change in the distribution of the coaxiality  
324 measure as the rotational speed of the drum increases over the test space. At  
325 low rotational speeds there appear to be two groups of volumetric elements:  
326 those with a high measure of coaxiality ( $\theta > 10^\circ$ ) and those with a very low  
327 measure of coaxiality ( $\theta \sim 1^\circ$ ). As the rotational speed increases, the group of  
328 volumetric elements with a larger measure of coaxiality diminishes in size, the  
329 measure of coaxiality for this group also decreases and finally appears to merge  
330 with the other group in the 56 rpm simulation. At the same time the group of  
331 volumetric elements with a small measure of coaxiality increases in size as the  
332 rotational speed increases. Most of the volumetric elements for the 56 and 63  
333 rpm simulations have  $\theta \sim 1^\circ$ .

## 334 6.2. Colinearity

335 The colinearity condition requires that the corresponding principle values of  
336 the shear stress  $\boldsymbol{\tau}$  and the symmetric velocity gradient  $\boldsymbol{D}$  scale by the same  
337 amount, i.e.

$$\frac{\xi_1}{\delta_1} = \frac{\xi_2}{\delta_2} = \frac{\xi_3}{\delta_3}. \quad (34)$$

338 Figure 13 shows the ratio between the corresponding principal directions of  $\boldsymbol{\tau}$   
339 and  $\boldsymbol{D}$  in the plane of rotation of the drum for all of the bins in all of the  
340 simulations performed.

341 From the figure it is apparent that almost all of the volumetric elements have  
 342  $\frac{\xi_1}{\delta_1} = \frac{\xi_2}{\delta_2}$ , regardless of the measure of coaxiality  $\theta$ . Since most of the volumetric  
 343 elements satisfy the second condition for isotropy (as mentioned in Section 6.1),  
 344 the measure of coaxiality  $\theta$  is therefore an appropriate measure for the isotropy  
 345 of the systems in the test space.

## 346 7. Friction coefficient

The results from the previous sections show that the rotating drum system becomes more isotropic as the rotational speed increases. The next step in examining the constitutive law of Jop et al. [11] is to investigate the effective friction  $\mu(I)$ . da Cruz et al. [5] found a linear relationship between  $\mu$  and  $I$ , given by

$$\mu(I) = \mu_{\min} + bI, \quad (35)$$

347 with constants  $\mu_{\min} \simeq 0.25$  and  $b \simeq 1.1$ . Jop et al. [10] found a sigmoidally-  
 348 shaped relation given by Equation 3.

349 In order to model the system as an incompressible fluid, a basic assumption  
 350 of Jop et al.'s law is in the neglecting of the small variation ( $< 10\%$ ) in the  
 351 packing fraction observed in the dense regime. Figure 14 shows a similar small  
 352 variation in packing fraction.

353 Figures 15 and 16 show the friction coefficient  $\mu$  versus the inertial number  
 354  $I$  for all of the bins in the test space, with the points being coloured by the  
 355 coaxiality measure  $\theta$ . Figure 15 shows the data with a log-scale for  $I$  and  
 356 Figure 16 shows the data with a linear-scale for  $I$ .

357 Figure 16 shows that for large values of inertial number ( $I > 10^{-1}$ ) the  
 358 effective friction  $\mu(I)$  is approximately linear. In Figure 15 it appears that  $\mu$  is  
 359 linear for small values of  $I$ , i.e.  $\mu(I) = c + d \log(x)$ . Based on these observations

360 the following effective friction is proposed:

$$\mu(I) = c + d \log(x) + ex, \quad (36)$$

361 where  $c$ ,  $d$  and  $e$  are constants.

362 Figures 15 and 16 also show the least-squares fit of the linear  $\mu(I)$  of da  
363 Cruz et al. [5], the sigmoidal  $\mu(I)$  of Jop et al. [10] and the  $\mu(I)$  proposed above  
364 (Equation 36). The least-squares fit parameters for the sigmoidal  $\mu(I)$  found  
365  $\mu_1 = \tan(24.4^\circ) \pm \tan(0.1^\circ)$ ,  $\mu_2 = \tan(51.6^\circ) \pm \tan(1.8^\circ)$ ,  $I_0 = 0.261 \pm 0.017$  and  
366 the root-mean-squared error  $\text{RSME} = 0.0623$ . The linear least-squares fit of  
367  $\mu(I)$  found the intercept  $\mu_{\min} = \tan(25.4^\circ) \pm \tan(0.1^\circ)$  and slope  $b = 1.65 \pm 0.02$   
368 with  $\text{RMSE} = 0.0675$ .

369 The least-squares fit of Equation 36 found  $c = 0.591 \pm 0.005$ ,  $d = 0.020 \pm 0.001$   
370 and  $e = 1.19 \pm 0.02$  with  $\text{RMSE} = 0.0609$ .

371 The RMSE for the newly proposed law is the lowest of the three fitted laws.  
372 The RMSE for the sigmoidal law of Jop et al. [11] is smaller than the linear law.  
373 All three laws capture the linear shape of the higher inertial number ( $I > 10^{-1}$ ).  
374 The new law appears to capture the behaviour for lower  $I$  better than the other  
375 two.

## 376 8. Discussion and conclusion

377 DEM-based simulations of spherical particles in a rotating drum were used  
378 to investigate scaling laws and constitutive relations for dense granular flow.  
379 Nine different simulations were run with the rotational speed varying evenly  
380 from 7 to 63 revolutions per minute. Spatio-temporal averaging techniques  
381 were used to extract kinematic and kinetic quantities from the resulting data.  
382 All nine simulations were found to be largely incompressible, confirming the  
383 incompressibility assumption of Jop et al. [11] for most regions of the flow.

384 A novel measure for isotropy in granular systems was proposed. The measure  
 385 is the angular difference between the nearest principle directions of the shear  
 386 stress and symmetric velocity gradient tensors. 3D rotating drum granular  
 387 flows seem to become more isotropic than their 2D counterparts, as confirmed  
 388 quantitatively by Figures (9 & 12) for a relatively low drum speed. Fluctu-  
 389 ations about the incompressibility state in the flowing layer, Figure 5, seem to  
 390 improve coaxiality from 2D to 3D, Figure 9. This is consistent with Heyman  
 391 et al.’s observation that compressibility is physical and can serve to regularise  
 392 the  $\mu(I)$ -rheology equations by extending their well-posedness in the flowing  
 393 layer. However, Figure 6 depicts negligible volume changes in the flowing layer,  
 394 suggesting that Heyman et al.’s requirement of volume changes associated with  
 395 sufficient dissipation is not the primary driver of the isotropy. The non-zero volu-  
 396 metric components  $\mathbf{D}_{\text{vol}}$  at the bottom of the drum, Figure 6, is arguably more  
 397 inline with Heyman et al.’s reasoning. Clearly, not all of the volume changes are  
 398 desirable as evidenced by the non-monotonic variation of the friction coefficient  
 399 with inertial number observed in Figure 16 at the very low inertial numbers—  
 400 Some of the volume changes are too aggressive, leading to gross instability of  
 401 the rheology equations. The non-monotonicity is suggestive of shear banding  
 402 which can imply a non-local rheology at play in the lowest regions of the drum.  
 403 Notwithstanding, the friction coefficient for the majority of the volumetric ele-  
 404 ments in the 3D simulations collapse onto a single curve in contrast to Cortet  
 405 et al. [3] who found no agreement for 2D drum simulations that incorporate  
 406 Jop et al.’s  $\mu(I)$ -rheology. It is also worth noting that these observations are  
 407 consistent with Barker et al. [2] who assert that the  $\mu(I)$ -rheology is likely to  
 408 be somewhat better posed in 3D. Notwithstanding the apparent complexity at  
 409 play in 3D rotating drum flows, the overall conclusion is that 3D rotating drum  
 410 systems facilitate enough compressibility to recover more coaxiality, which in

411 turn, restores greater stability to the governing equations over a wider range  
412 of the flow than the equivalent 2D case. A full stability analysis is beyond the  
413 scope of this paper and will be explored in future work.

414 Finally, the phenomenological laws of da Cruz et al. [5] and Jop et al. [10]  
415 were compared with an empirical relation proposed here. The new relation was  
416 found to fit the data better, with the sigmoidal law of Jop et al. being the  
417 next-best. While the three models may fit the data for higher inertial numbers,  
418 it is apparent that for lower inertial numbers ( $I < 10^{-2}$ ) they do not capture  
419 the behaviour accurately. The friction coefficient appears to diverge for lower  
420 inertial numbers and takes on a “hook”-like shape. For some inertial numbers in  
421 the range  $I < 10^{-2}$  there are multiple possible values of the friction coefficient,  
422 suggesting that the equations governing the  $\mu(I)$ -rheology finally succumb to  
423 the instability of an ill-posed system. This is most likely due to shear-banding  
424 effects observed in regions with quasi-static flow. Future work will aim to isolate  
425 the source of the flow instability at the bottom of the drum and, possibly, testing  
426 it with non-local rheologies.

#### 427 **Declaration of Competing Interest**

428 The authors declare that they have no known competing financial interests or  
429 personal relationships that could have appeared to influence the work reported  
430 in this paper.

#### 431 **Funding**

432 The National Research Foundation and the Centre for Minerals Research at  
433 the University of Cape Town are acknowledged for funding TP.

434 **References**

435 **References**

- 436 [1] Andreotti, B., Forterre, Y., Pouliquen, O., 2013. Granular Media: Between  
437 Fluid and Solid. Cambridge University Press.
- 438 [2] Barker, T., Schaeffer, D., Bohorquez, P., Gray, J., 2015. Well-posed and  
439 ill-posed behaviour of the  $\mu$ -rheology for granular flow. Journal of Fluid  
440 Mechanics 779, 794–818. doi:[10.1017/jfm.2015.412](https://doi.org/10.1017/jfm.2015.412).
- 441 [3] Cortet, P.P., Bonamy, D., Daviaud, F., Dauchot, O., Dubrulle, B., Ren-  
442 ouf, M., 2009. Relevance of visco-plastic theory in a multi-directional in-  
443 homogeneous granular flow. Europhysics Letters 88, 14001. doi:[10.1209/  
444 0295-5075/88/14001](https://doi.org/10.1209/0295-5075/88/14001).
- 445 [4] Cundall, P., 1971. A computer model for simulating progressive, large-scale  
446 movements in blocky rock systems., in: Proceedings of the International  
447 Society for Rock Mechanics.
- 448 [5] da Cruz, F., Emam, S., Prochnow, M., Roux, J.N., Chevoir, F., 2005.  
449 Rheophysics of dense granular materials: Discrete simulation of plane shear  
450 flows. Physical Review E 72, 021309. doi:[10.1103/PhysRevE.72.021309](https://doi.org/10.1103/PhysRevE.72.021309).
- 451 [6] Forterre, Y., Pouliquen, O., 2008. Flows of dense granular media. Annu.  
452 Rev. Fluid Mech. 40, 1–24. doi:[10.1146/annurev.fluid.40.111406.  
453 102142](https://doi.org/10.1146/annurev.fluid.40.111406.102142).
- 454 [7] GDR MiDi, 2004. On dense granular flows. European Physical Journal E  
455 14, 341–365. doi:[10.1140/epje/i2003-10153-0](https://doi.org/10.1140/epje/i2003-10153-0).
- 456 [8] Goldhirsch, I., 2003. Rapid granular flows. Annual Review of Fluid Mech-  
457 anics 35, 267–293. doi:[10.1146/annurev.fluid.35.101101.161114](https://doi.org/10.1146/annurev.fluid.35.101101.161114).

- 458 [9] Heyman, J., Delanney, R., Tabuteau, H., Valance, A., 2017. Compressibil-  
459 ity regularizes the  $\mu(I)$ -rheology of dense granular flows. *Journal of Fluid*  
460 *Mechanics* 830, 553–568. doi:<https://doi.org/10.1017/jfm.2017.612?>
- 461 [10] Jop, P., Forterre, Y., Pouliquen, O., 2005. Crucial role of sidewalls in  
462 granular surface flows: consequences for the rheology. *Journal of Fluid*  
463 *Mechanics* 541, 167–192. doi:[10.1017/S0022112005005987](https://doi.org/10.1017/S0022112005005987).
- 464 [11] Jop, P., Forterre, Y., Pouliquen, O., 2006. A constitutive law for dense  
465 granular flows. *Nature* 441, 727–730. doi:[10.1038/nature04801](https://doi.org/10.1038/nature04801).
- 466 [12] Lagrée, P.Y., Staron, L., Popinet, S., 2011. The granular column collapse  
467 as a continuum: validity of a two-dimensional navier-stokes model with a  
468  $\mu(i)$ -rheology. *Journal of Fluid Mechanics* 686, 378–408. doi:[10.1017/jfm.](https://doi.org/10.1017/jfm.2011.335)  
469 [2011.335](https://doi.org/10.1017/jfm.2011.335).
- 470 [13] Pouliquen, O., Chevoir, F., 2002. Dense flows of dry granular mater-  
471 ial. *Comptes Rendus Physique* 3, 163–175. doi:[10.1016/S1631-0705\(02\)](https://doi.org/10.1016/S1631-0705(02)01309-9)  
472 [01309-9](https://doi.org/10.1016/S1631-0705(02)01309-9).
- 473 [14] Pournin, L., Liebling, T.M., Mocellin, A., 2001. Molecular-dynamics force  
474 models for better control of energy dissipation in numerical simulations  
475 of dense granular media. *Physical Review E* 65, 011302. doi:[10.1103/](https://doi.org/10.1103/PhysRevE.65.011302)  
476 [PhysRevE.65.011302](https://doi.org/10.1103/PhysRevE.65.011302).
- 477 [15] Roux, J.N., Combe, G., 2002. Quasistatic rheology and the origins of strain.  
478 *Comptes Rendus Physique* 3, 131–140. doi:[10.1016/S1631-0705\(02\)](https://doi.org/10.1016/S1631-0705(02)01306-3)  
479 [01306-3](https://doi.org/10.1016/S1631-0705(02)01306-3).
- 480 [16] Rycroft, C., Kamrin, K., Bazant, M., 2009. Assessing continuum postulates  
481 in simulations of granular flow. *Journal of the Mechanics and Physics of*  
482 *Solids* 57, 828 – 839. doi:[10.1016/j.jmps.2009.01.009](https://doi.org/10.1016/j.jmps.2009.01.009).

- 483 [17] Schaeffer, D., 1987. Instability in the evolution equations describing in-  
484 compressible granular flow. *Journal of Differential Equations* 66, 19 – 50.  
485 doi:[10.1016/0022-0396\(87\)90038-6](https://doi.org/10.1016/0022-0396(87)90038-6).
- 486 [18] Smilauer, V., Catalano, E., Chareyre, B., Dorofeenko, S., Duriez, J., Dyck,  
487 N., Elias, J., Er, B., Eulitz, A., Gladky, A., Guo, N., Jakob, C., Kneib,  
488 F., Kozicki, J., Marzougui, D., Maurin, R., Modenese, C., Scholtes, L.,  
489 Sibille, L., Stransky, J., Sweijen, T., Thoeni, K., Yuan, C., 2015. *Yade*  
490 *Documentation* 2nd ed. Zenodo. doi:[10.5281/zenodo.34073](https://doi.org/10.5281/zenodo.34073).
- 491 [19] Staron, L., Lagree, P.Y., Popinet, S., 2012. The granular silo as a continuum  
492 plastic flow: The hour-glass vs the clepsydra. *Physics of Fluids* 24, 103301.  
493 doi:[10.1063/1.4757390](https://doi.org/10.1063/1.4757390).

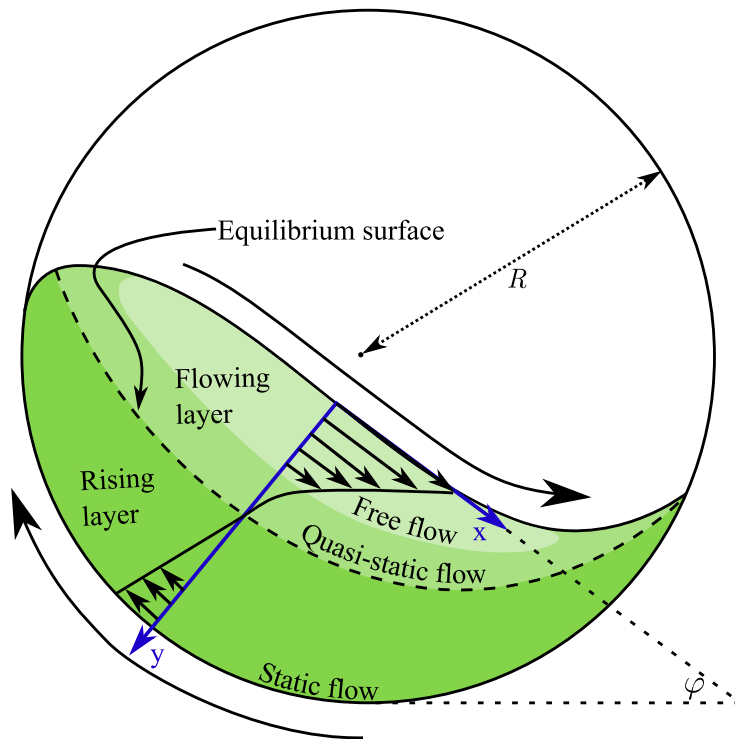


Figure 1: Regions of flow in a rolling or cascading rotating drum.  $R$  is the radius of the drum, the orthonormal coordinate system  $(x, y)$  used in some scaling laws is shown in blue. Lastly, the angle of repose  $\varphi$  is shown.

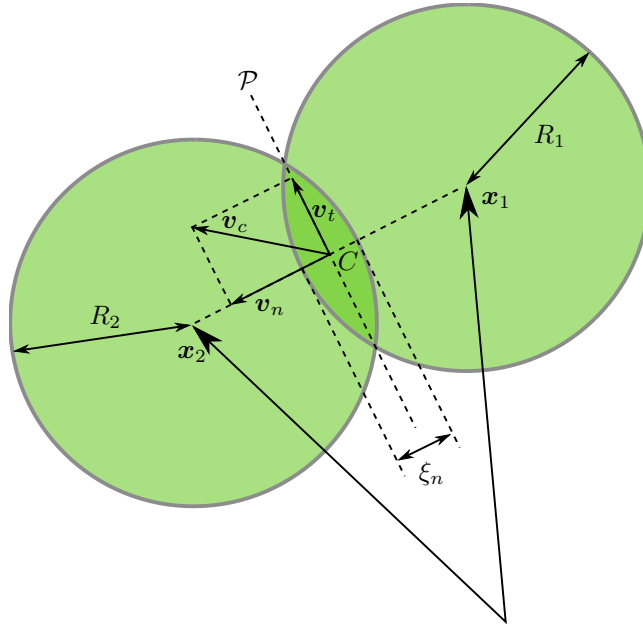


Figure 2: Diagram for two spherical particles in contact.

Material parameter	Drum	“Glass” beads
Friction coefficient $\mu$	0.95	0.5
Normal restitution coefficient $\delta_n$	0.46	0.56
Tangential restitution coefficient $\delta_t$	0.46	0.46
Duration of contact $t_c$	$10^{-4}$ s	$10^{-4}$ s

Table 1: The parameters for the two types of materials in the DEM simulations.

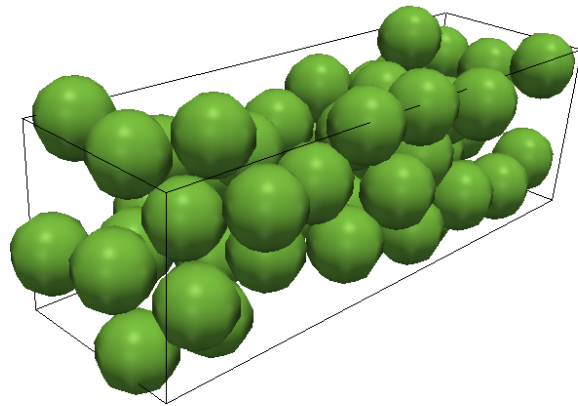


Figure 3: A volumetric element with spheres inside.

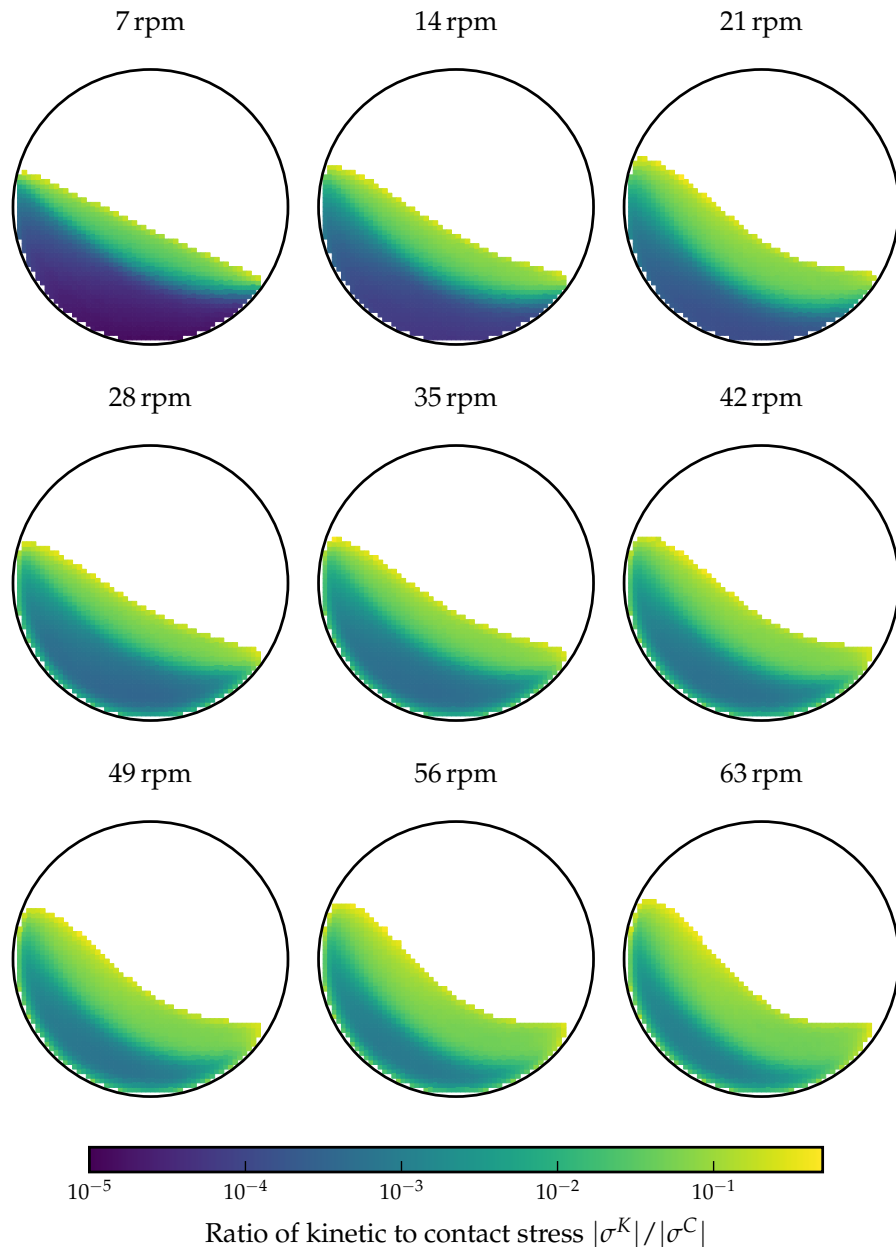


Figure 4: The ratio of the kinetic stress  $\sigma^k$  to contact stress  $\sigma^c$  over the test space. The colourmap is log-scaled.

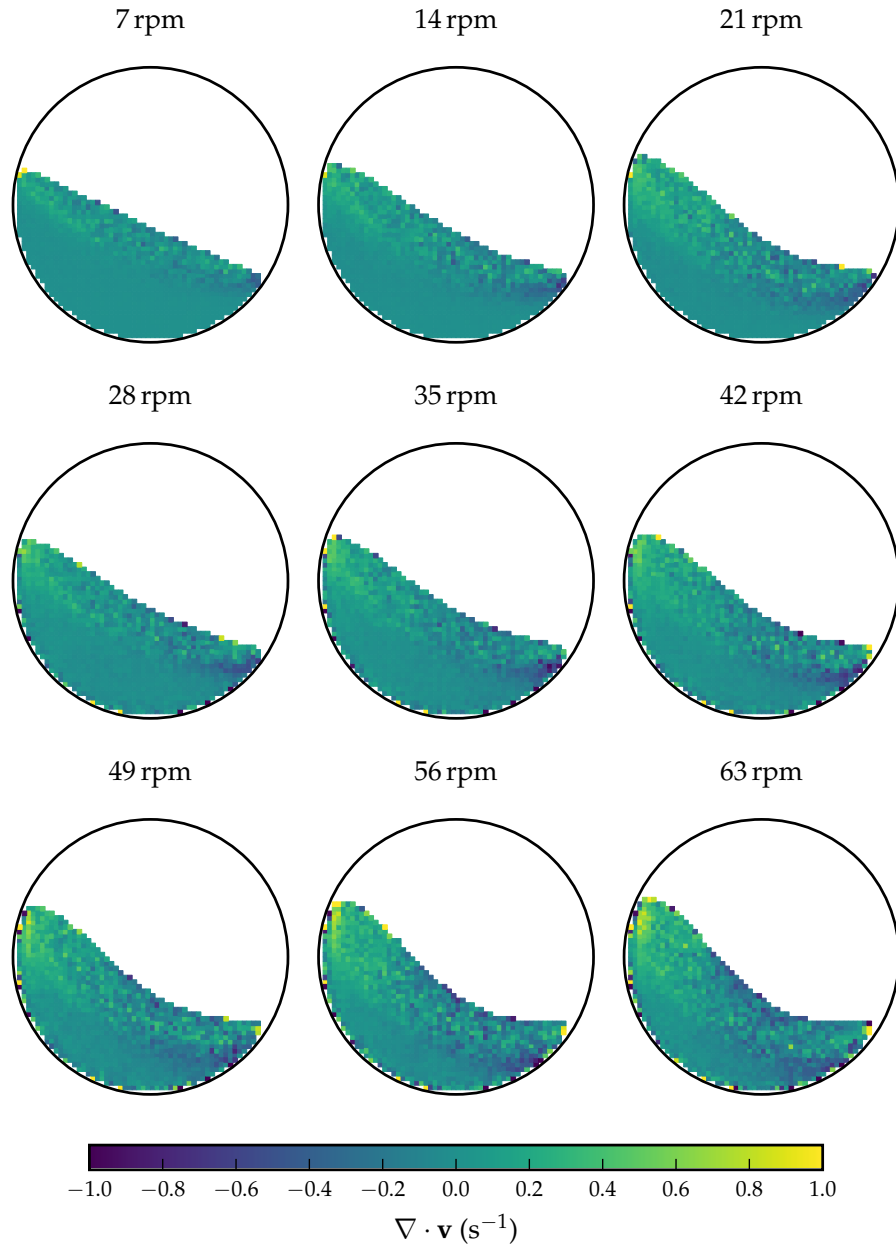


Figure 5: The divergence of the velocity  $\nabla \cdot \mathbf{v}$  over the test space. The colourbar is truncated from  $-1$  to  $1$  as there are several volumetric elements with very high magnitude of  $\nabla \cdot \mathbf{v}$ . These results are spurious, as they arise from partially-filled volumetric elements at the free surface.

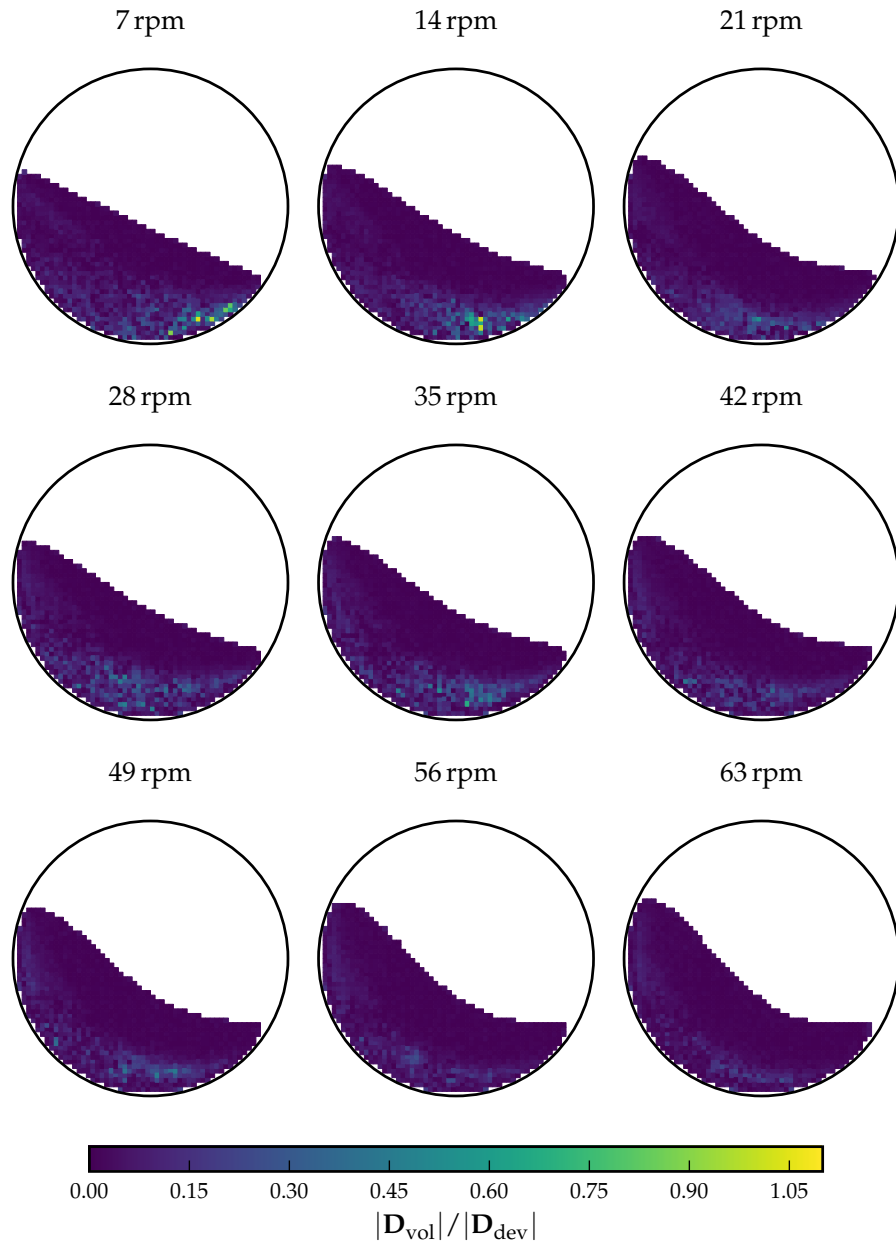


Figure 6: The ratio of the volumetric and deviatoric components of the symmetric velocity gradient  $|\mathbf{D}_{\text{vol}}|/|\mathbf{D}_{\text{dev}}|$  over the test space.

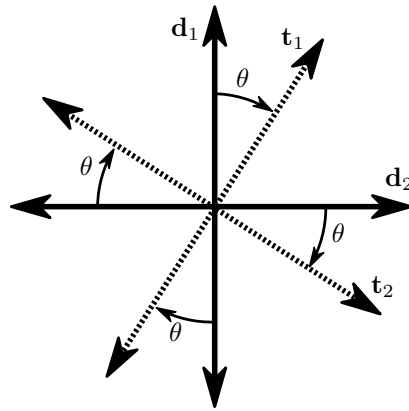


Figure 7: A diagram illustrating the measure of coaxiality  $\theta$ , which is obtained by finding the smallest angular difference between the principal directions  $t_i$  and  $d_i$  of  $D$  and  $\tau$  respectively in the plane of rotation of the drum.

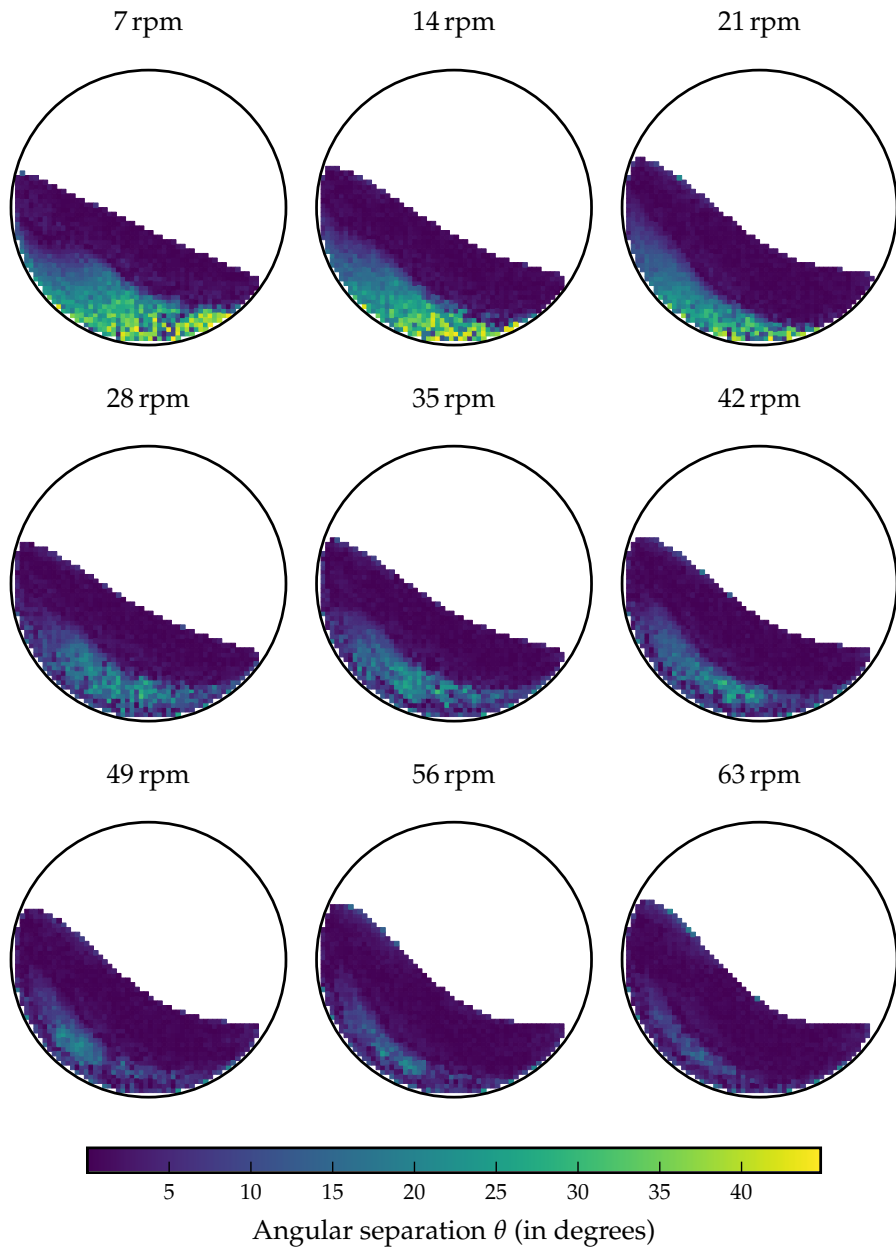


Figure 8: The measure of coaxiality  $\theta$  over the test space.

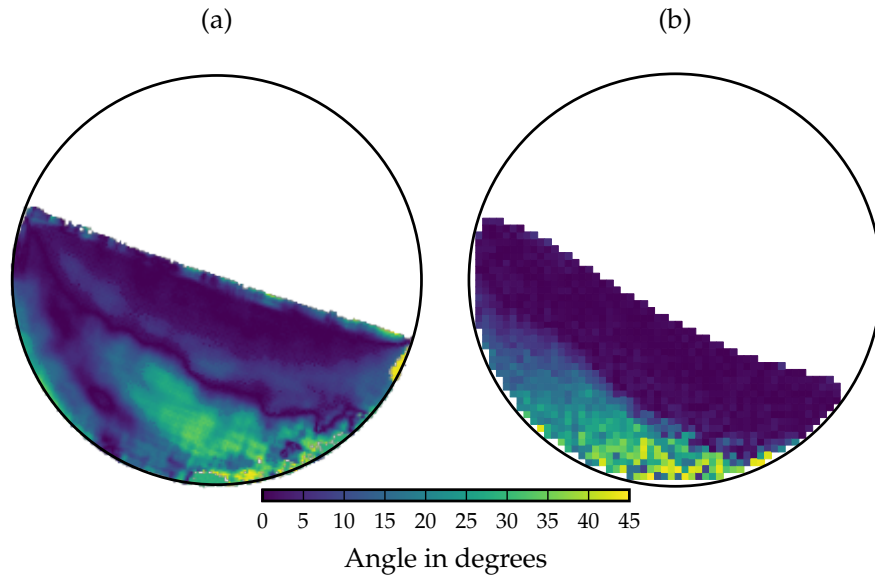


Figure 9: The measure of coaxiality from (a) the 12 rpm simulation of Cortet et al. [3] (b) the 14 rpm simulation in this work. In order to get a better qualitative comparison, the data for (a) was extracted digitally from Figure 6a of Cortet et al. [3] and converted to the same colour map as (b).

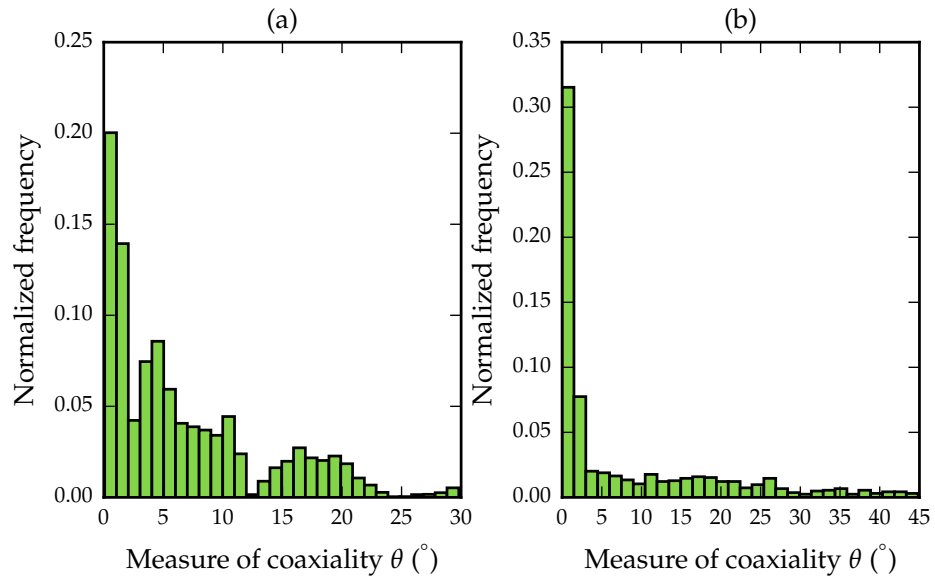


Figure 10: Histograms showing the normalized frequency of the measure of coaxiality  $\theta$  for (a) the 12 rpm simulation of Cortet et al. [3] and (b) the 14 rpm simulation in this work. The data for (a) was digitally extracted from Figure 6a of Cortet et al. [3].

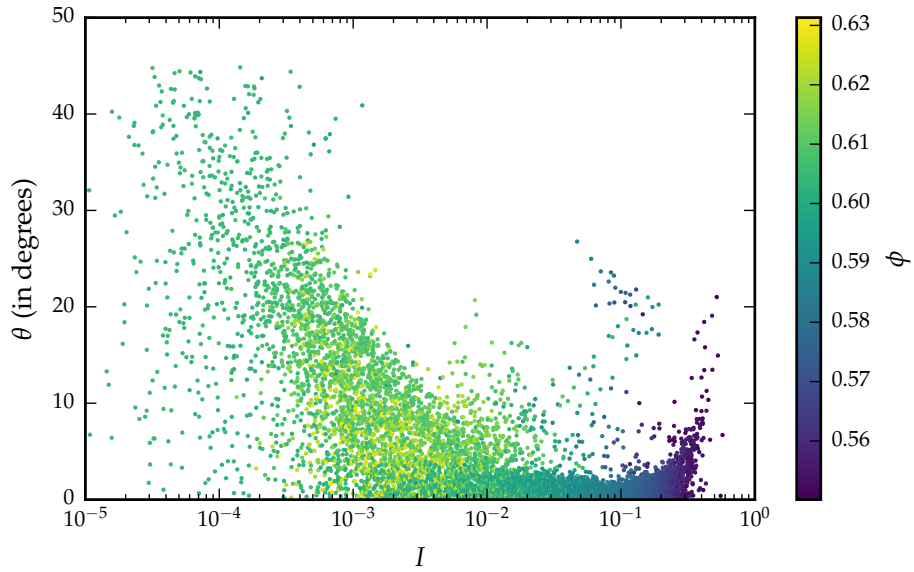


Figure 11: The measure of coaxiality  $\theta$  vs the inertial number  $I$  over the test space. The points are coloured by the packing fraction  $\phi$ .

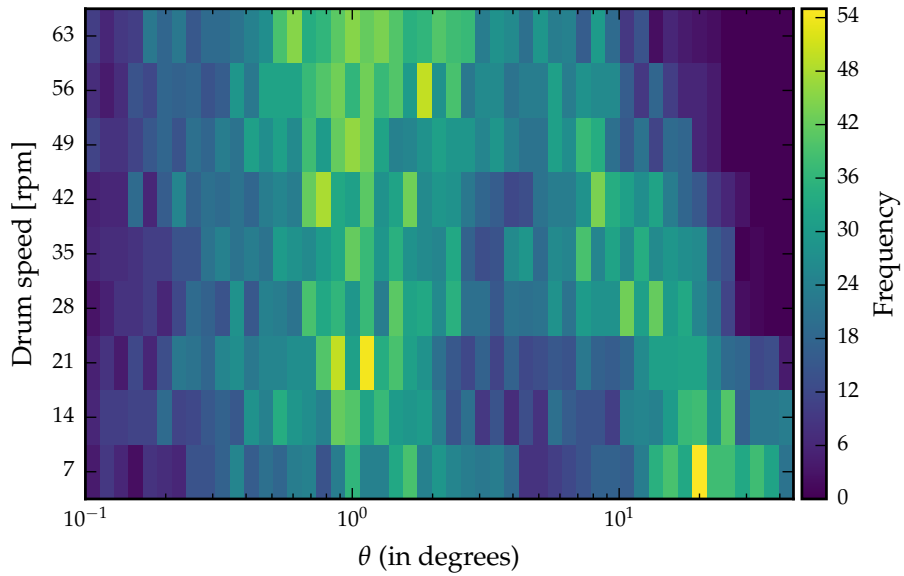


Figure 12: A set of histograms of the measure of coaxiality  $\theta$ . Each row of cells is a histogram for one of the simulations. From the bottom row upwards the rows are arranged in ascending order of rotational speed. The rotational speed is shown on the vertical axis. Each row/histogram is divided into 50 bins. The bins are equally spaced in log space. The frequency of volumetric elements in each bin is represented by the colour.

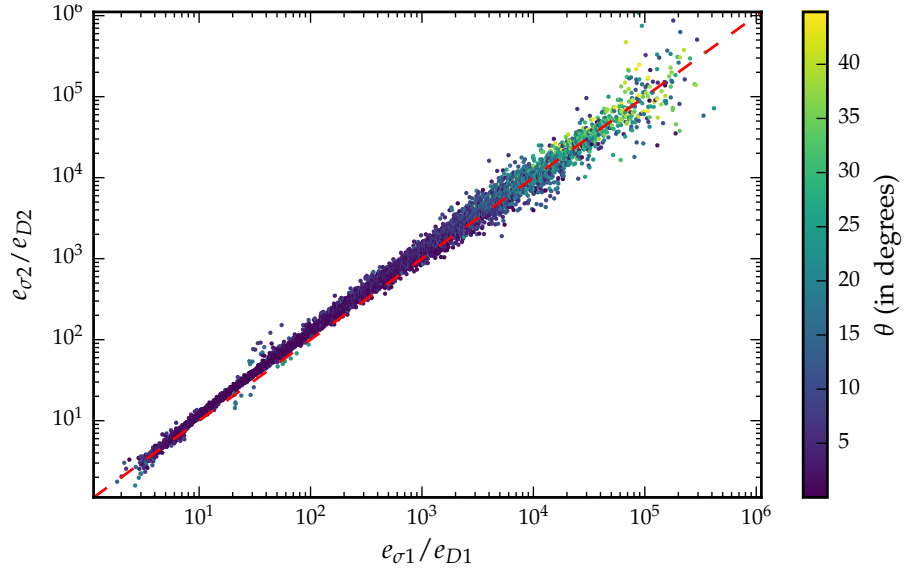


Figure 13: The scaling between the maximal principle directions of  $\boldsymbol{\tau}$  and  $\boldsymbol{D}$  for the volumetric elements in all of the simulations vs that of the minimal principle directions. The points are coloured by the measure of coaxiality  $\theta$ . For reference the line  $\frac{\xi_1}{\delta_1} = \frac{\xi_2}{\delta_2}$  is included.

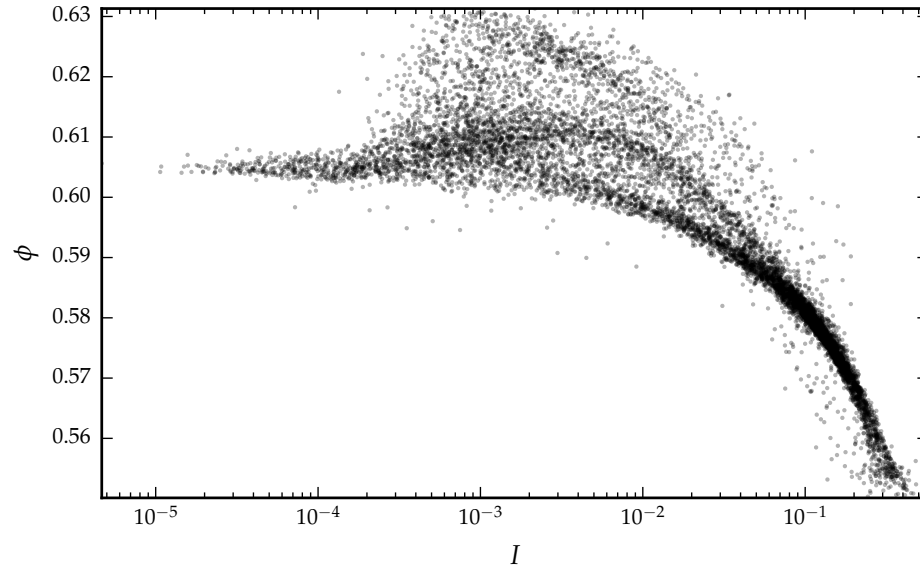


Figure 14: A log-linear plot of the packing fraction  $\phi$  versus the inertial number  $I$  over the test space.

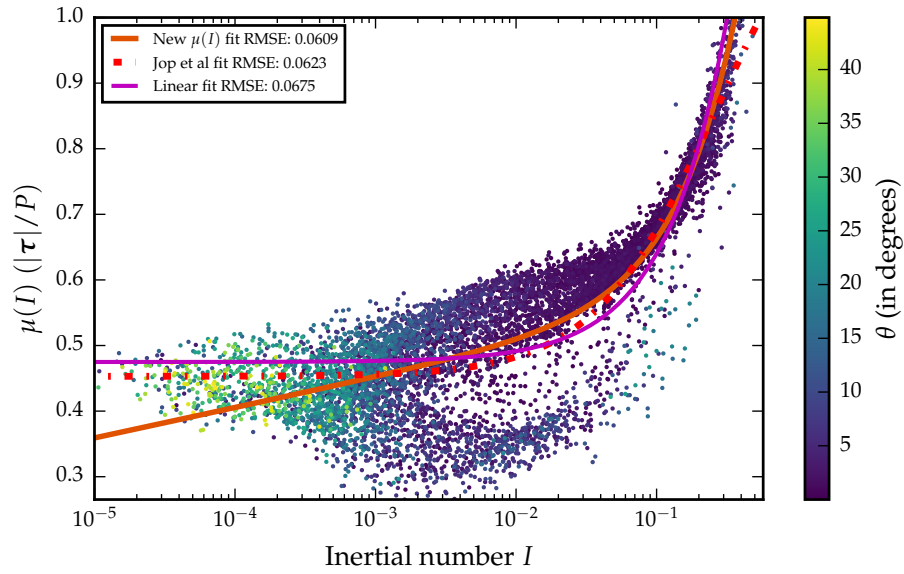


Figure 15: The friction coefficient  $\mu$  vs the inertial number  $I$  over the test space. The points are coloured by the measure of coaxiality  $\theta$ .

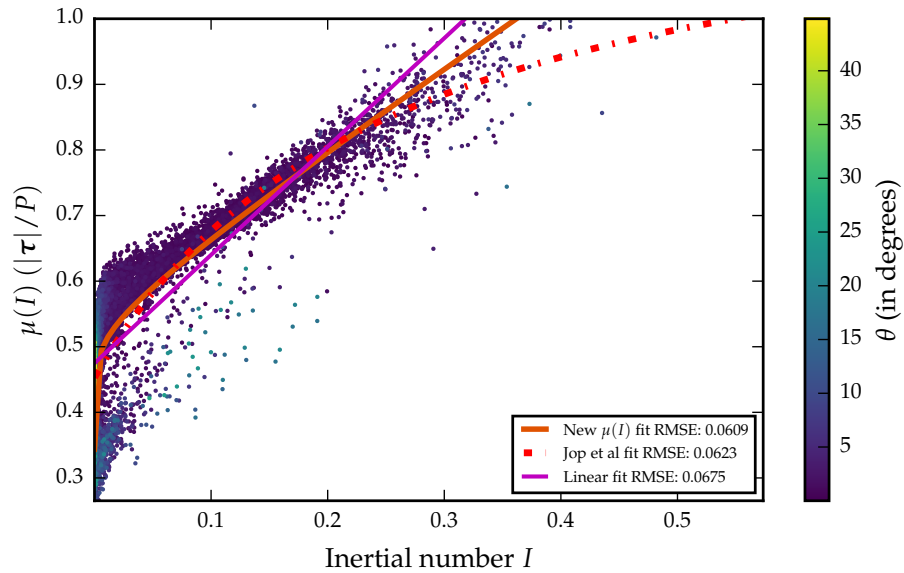


Figure 16: The friction coefficient  $\mu$  vs the inertial number  $I$ , with a log-scale, over the test space. The points are coloured by the measure of coaxiality  $\theta$